Nanoscale Structure and Microscale Stiffness of DNA Nanotubes

Daniel Schiffels,[†,‡] Tim Liedl,[‡] and Deborah K. Fygenson[†,*]

[†]Physics Department, University of California, Santa Barbara, California, United States, and [‡]Physik Department and CeNS, Ludwig-Maximilians-Universität, München, Germany

ABSTRACT We measure the stiffness of tiled DNA nanotubes (HX-tubes) as a function of their (defined) circumference by analyzing their micrometer-scale thermal deformations using fluorescence microscopy. We derive a model that relates nanoscale features of HX-tube architecture to the measured persistence lengths. Given the known stiffness of double-stranded DNA, we use this model to constrain the average spacing between and effective stiffness of individual DNA duplexes in the tube. A key structural feature of tiled nanotubes that can affect stiffness is their potential to form with discrete amounts of twist of the DNA duplexes about the tube axis (supertwist). We visualize the supertwist of HX-tubes using electron microscopy of gold nanoparticles, attached to specific sites along the nanotube. This method reveals that HX-tubes tend not to form with supertwist unless forced by sequence design, and, even when forced, supertwist is reduced by elastic deformations of the underlying DNA lattice. We compare the hybridization energy gained upon closing a duplex sheet into a tube with the elastic energy paid for deforming the sheet to allow closure. In estimating the elastic energy we account for bending and twisting of the individual duplexes as well as shearing between them. We find the minimum supertwist state has minimum free energy, and global untwisting of forced supertwist is energetically favorable, consistent with our experimental data. Finally, we show that attachment of Cy3 dyes or changing counterions can cause nanotubes to adopt a permanent writhe with micrometer-scale pitch and amplitude. We propose that the coupling of local twist and global counter-twist may be useful in characterizing perturbations of DNA structure.

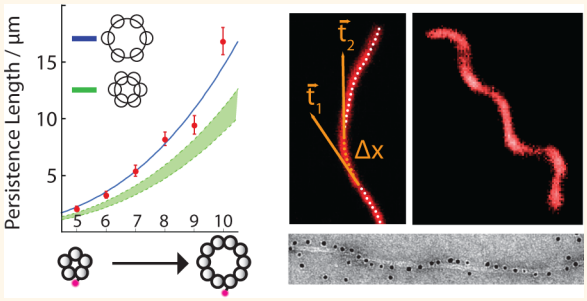

KEYWORDS: cyanine fluorophors · self-assembly · single-stranded tiles · ultrastructure · tangent correlation · twisting modulus · bending modulus · cork screw · colloidal AuNP

The ability to build structures of defined shapes and mechanical properties has always been a prerequisite for the development of new technologies. Modern research facilities, as well as the instruments used within those facilities, rely on a fundamental knowledge of how building materials such as steel or concrete behave mechanically. On the nanometer scale, self-assembly has proven to be a viable method for building structures with reliability and precision. At first an exotic discipline, DNA-based self-assembly[1] in particular has developed into an enabling technique that is finding application in such disparate fields as structural biology,[2−4] nanomedicine,[5,6] nanoelectronics,[7] plasmonics,[8,9] and single-molecule detection.[10−14] With the ever-increasing requirements DNA structures must fulfill in order to perform their tasks comes the need to carefully study the mechanical properties of their main building motifs. Just as steel and concrete construction could reach its present capacity and reliability only with advanced knowledge of the mechanical properties of those materials, a detailed understanding of the mechanical behavior of building motifs in DNA nanotechnology will boost the development of complex nanoscale architectures.

In many studies that employ DNA as a building block, DNA double helices are arranged in parallel to form multihelical bundles or sheets.[2,15−28] As a result, the persistence length of the DNA double helix is multiplied and micrometer-scale objects can be created. Parallel arrangements can be achieved by tile-assembly or by the scaffolded DNA origami approach. Previous work has shown that the stiffness of multihelical bundles can be estimated by approximating the DNA double helices as continuously connected cylinders of homogeneous material with isotropic Young's

* Address correspondence to deborah@physics.ucsb.edu.

Received for review March 18, 2013 and accepted July 10, 2013.

Published online July 23, 2013
10.1021/nn401362p

© 2013 American Chemical Society

moduli[15,18,20,28] but also that deviations from this picture can be observed.[20,29]

Given the very well studied material properties of double-stranded DNA,[30,31] the key parameter that determines bending stiffness of arrays of DNA helices is their second moment of inertia, *J*. We studied a set of DNA nanotubes of defined circumference (HX-tubes),[19] which allowed us to systematically vary *J* and measure the associated persistence length *P*. This approach confirmed that persistence length scales with the second moment of inertia and revealed structural features of DNA nanotubes such as the average helix spacing under solution conditions. The observed helix spacing is in good agreement with recent cryo-EM studies,[32] which provided a pseudoatomic model of a DNA origami structure.

Being tiled structures, HX-tubes can form with the DNA duplexes either parallel to or twisting about the tube axis in discrete amounts (supertwist). Geometrically, *J* and, therefore, *P* depend on the amount of supertwist. The single helix resolution, required to directly visualize supertwist, cannot be achieved by conventional transmission electron microscopy (TEM) or atomic force microscopy (AFM). We therefore characterized the supertwist by placing gold nanoparticles (AuNP) on a specific DNA helix of the tubes and tracking their position relative to the tube axis using TEM. This approach revealed that (i) HX-tubes tend not to form with supertwist unless forced by sequence design; (ii) thermally excited tube twist occurs on length scales much smaller than the persistence length; and (iii) the pitch of forced supertwist is much larger than geometrically expected.

To explain our observations, we propose an elastic cylinder model for DNA nanotubes. In the model, adjacent cylinders can shear with respect to each other at an elastic cost, associated with deforming the strand crossovers between them. We calculate the free energy gained upon closing a duplex sheet into a tube and show that it is minimized at the observed, minimum supertwist allowed by HX-tube sequence design. The model also predicts untwisting of forced supertwist and captures the observed supertwist pitch. We show that the low twist persistence length can be explained by cylinder shearing.

For applications such as drug delivery, not only are mechanical properties of DNA arrays important, but so are their robustness to changes in solution conditions and to the presence of molecular ligands. We observed that HX-tubes were stable and displayed micrometer-scale deformations of the tube axis, adopting a writhe shape when the ionic strength or the density of dye molecules was changed. Thus DNA nanotubes may be interesting tools to magnify nanoscale deformations of DNA molecules.

RESULTS AND DISCUSSION

In 2008, Yin and co-workers pioneered the use of "half-crossover" (HX) tiles and designed a set of DNA nanotubes with a defined number of B-form double helices in circumference, known as "*n*-helix tubes" or *n*HT.[19] To better understand HX-based structures and characterize the effective Young's modulus of dsDNA materials, we measured the stiffness of *n*HT with *n* ranging from 5 to 10.

We measured *n*HT stiffness in terms of *persistence length*, *P*, the length over which correlations in the orientation of a thermally fluctuating contour decay exponentially. To characterize their thermally fluctuating contours, we assembled *n*HT with one or more fluorescently labeled DNA strands, confined them to two dimensions between polymer-coated glass surfaces, and imaged them using fluorescence videomicroscopy.

In a two-dimensional system, *P* is defined by

$$\langle \hat{\mathbf{t}}(x) \cdot \hat{\mathbf{t}}(x + \Delta x) \rangle = e^{-\Delta x/2P} \quad (1)$$

where $\langle \hat{\mathbf{t}}(x) \cdot \hat{\mathbf{t}}(x + \Delta x) \rangle$, called the tangent correlation, is the average inner product between two unit tangent vectors separated by a distance Δx along a contour (Figure 1a). We used an automated tracing algorithm[33]

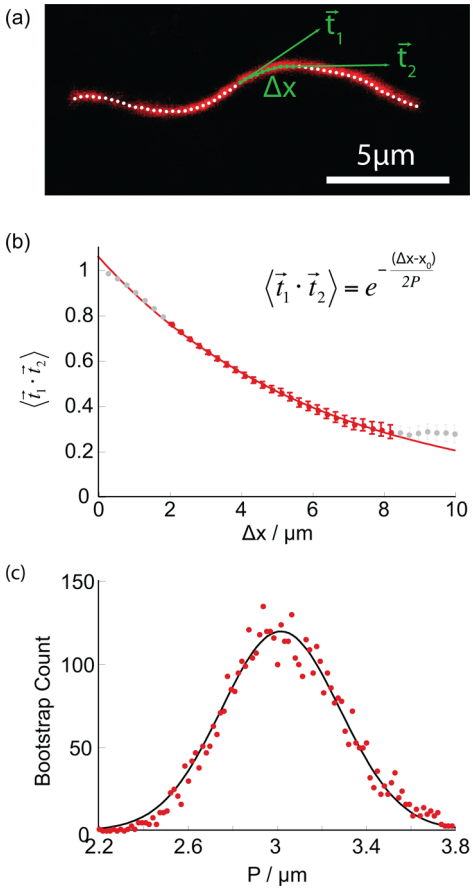

Figure 1. Calculation of persistence length from a set of contours: (a) Typical fluorescence image of a DNA nanotube with its trace superimposed, indicating two tangents, t_1 and t_2, and their separation distance Δx. (b) Tangent correlation function with a curve fit of eq 2. Data plotted in gray are outside the fit limits. (c) Persistence length distribution obtained by a bootstrap method and its least-squared-error fit to a Gaussian profile.

to assign coordinates to a set of points along a contour, spaced every 4 pixels (~0.25 μm) between manually selected start and end points. We then used a home-made Matlab script to calculate the tangent correlation as a function of Δx from the trace coordinates.

A deviation from exponential dependence was present at the smallest and largest Δx in every data set (Figure 1b). At large Δx, it takes more time for the tangents of a given nanotube to randomize. To avoid relying on the ~100 conformations from a single (longest) tube, we set an upper bound, $\Delta x < \Delta x_{max}$, by excluding tangent correlations for which there were less than 500 tangent pairs in the data set. At small Δx, tangents were excessively correlated due to the finite thickness of the sample volume ($\lesssim$2 μm), which accommodates small-amplitude fluctuations perpendicular to the image plane. We therefore obtained the persistence length by fitting a modified version of eq 1:

$$\langle \hat{\mathbf{t}}(x) \cdot \hat{\mathbf{t}}(x + \Delta x) \rangle = e^{-(\Delta x - x_0)/2P} \quad (2)$$

and restricting the data to $\Delta x > 2$ μm.

We estimated the uncertainty in P using a bootstrap method: from the full set of contours ($167 < U < 844$) for a given nHT, a subset U_i was randomly chosen (with replacement) and its persistence length P_i obtained. As this process is repeated (typically 5000 times), the mean of P_i approaches the value of P obtained using the full contour set, and the standard deviation, σ_P, provides an estimate of the uncertainty in the measurement of P. The uncertainty was uniformly $\leq$10% of P and not sensitive to the sample size (Table 1).

We find that P increases with n, as expected (Table 1). To interpret $P(n)$ quantitatively in terms of nHT structure, we model each double helix as an elastic cylinder of radius r and Young's modulus y, and each nanotube as an array of such cylinders uniformly spaced along the circumference of a circle with radius R.

The persistence length of a cylinder is

$$p = \frac{y}{k_B T} j \quad (3)$$

where $j = \pi r^4/4$ is the area moment of inertia and $k_B T$ is the thermal energy, the product of the temperature, T, and Boltzmann's constant, k_B. Similarly, the persistence length of a nanotube is

$$P = \frac{Y}{k_B T} J \quad (4)$$

where Y is the effective Young's modulus of dsDNA in the nanotube and J is its area moment of inertia. Given the spacing between neighboring helices, $s = 2R \sin(\pi/n)$ (for $n > 2$), J can be calculated from j using the parallel axis theorem. The result,

$$P = np\left(\frac{Y}{y}\right)\left[1 + 2\left(\frac{R}{r}\right)^2\right] = np_{eff}\left[1 + \frac{(s/r)^2}{2\sin^2(\pi/n)}\right] \quad (5)$$

is independent of the angle at which the neutral axis bisects the nanotube (Section 4, Supporting Information). Here we define $p_{eff} = (Y/y)p$ to be the effective persistence length of a DNA double helix within the tube.

In previous work, it has been assumed that complete crossovers (in which two DNA strands exchange between neighboring helices) do not change the effective Young's modulus of dsDNA ($Y = y$) and that the double helices are tighly packed ($s = 2r$).[15,18,20,28] With these assumptions, eq 5 reduces to

$$P = np\left[1 + \frac{2}{\sin^2(\pi/n)}\right] \quad (6)$$

Fitting eq 6 to our data with p as a free parameter yields an estimate of $p = 65 \pm 2$ nm. However, measurements of the persistence length of dsDNA consistently find $p \lesssim 50$ nm near room temperature.[34] Under conditions like ours, with high Mg^{2+} concentration and a high density of backbone nicks, values closer to 40 nm are reported.[35,36] Figure 2a plots eq 6 for 40 nm $< p <$ 50 nm (shaded region) alongside our measurements (red points), making it clear that, given realistic values for the persistence length of dsDNA, eq 6 underestimates nHT stiffness.

The most likely explanation is that the double helices are not tightly packed ($s > 2r$). DNA duplexes have been observed bowing away from one another between complete crossovers in DNA nanostructures.[19,24,27,32] The reported distance between the centers of neighboring duplexes ranges from 2.6 nm, measured by cryo-EM,[27,32] to 3.0 nm, measured by AFM.[24] This separation is presumably due to electrostatic repulsion between phosphates along the DNA backbones of neighboring helices.

Fitting eq 5 to our data does not identify a unique set of values for s and p_{eff}. Taking the reported values of s as bounds yields a range of 32 nm $< p_{eff} <$ 45 nm. For s = 2.8 nm, in the middle of the reported range, p_{eff} = 38 $\pm$ 1 nm, and the resulting function is plotted as a solid line in Figure 2a. Best fit functions for all other

TABLE 1. Persistence Lengths of nHT and Characteristics of the Data Sets from Which They Are Derived

	n (helices)	P (μm)	σ_P (μm)	x_o (μm)	Δx_{max} (μm)	N (tubes)	U (contours)
5HT	5	2.0	0.2	0.34	2.3	5	167
6HT	6	3.3	0.3	0.24	6.7	13	503
7HT	7	5.4	0.5	0.57	4.9	7	212
8HT	8	8.2	0.6	0.62	7.9	5	377
9HT	9	9.4	0.8	0.69	7.7	5	336
10HT	10	16.8	1.2	0.50	13.8	13	844
$6HT_2$	6	2.1	0.2	0.61	3.3	10	269
$6HT_{3Cy3}$	6	2.7	0.3	0.00	4.4	4	306

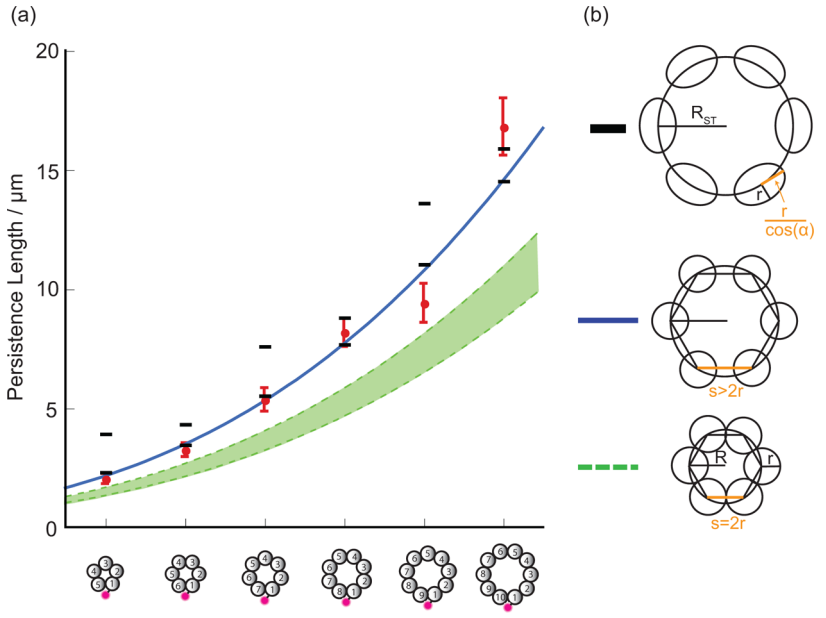

Figure 2. Persistence length of *n*-helix tubes. (a) Red dots and error bars: measured data. Dashed curves and shaded region: close-packed model (s = 2.1 nm) with 40 nm < p < 50 nm. Solid curve: weighted least-squared-error fit of eq 5 with s = 2.8 nm yields p_{eff} = 38 ± 1 nm. Black bars: calculated persistence lengths for s = 2.8 nm, p_{eff} = 38 nm, and supertwist (shown are ST_0, ST_2 for even-*n*HT, ST_1 and ST_3 for odd-*n*HT). (b) Illustration of the cross-section of a 6HT for close-packed tubes (bottom), swollen tubes (middle) and supertwisted swollen tubes (top).

values of s look the same: they fit well to measurements of 5HT through 8HT, but they overestimate the stiffness of 9HT and underestimate the stiffness of 10HT.

Tangent correlation analysis on the contour sets of individual *n*HTs showed that tubes with the same number of helices may have significantly different persistence lengths (Tables S1 and S2, Supporting Information). In the case of 9HT, four of the five individual contour sets yielded persistence lengths between 9.9 and 13.6 μm. The fifth nanotube was significantly more flexible (P = 5.5 ± 1.1 μm). Among individual 10HT, nine of the 13 individual contour sets yielded persistence lengths consistent with 14.5 μm, the value predicted by the fit. The other four nanotubes were significantly stiffer, with an average persistence length of 22.2 μm.

Structural differences among nanotubes of the same circumference, which may underlie these deviations, could result from the repetitive nature of the tile DNA lattice. This lattice structure makes it possible for an open sheet of interwoven duplexes to close into a tube with any number of discrete offsets along the edge (Figure 3). If ℓ_0 is the sequence repeat length (21 base pairs = 2 helical turns ≈ 7.14 nm), the allowed edge offsets q are given by

$$q_{even} = (2m)\frac{\ell_0}{2};\ q_{odd} = (2m-1)\frac{\ell_0}{2} \qquad (7)$$

for even and odd numbers of duplexes in the sheet, respectively, where m is an integer. Notice that even-*n*HT can form with no edge offset, but odd-*n*HT contain a seam, between the first and *n*th strands, along which the duplex sheet must shear in order for the bonding strands to hybridize. Whenever a sheet closes with finite edge offset, the duplexes follow a helical path about, rather than align parallel to, the axis of the nanotube (Figure 3c). We refer to nanotubes with such helical double helices as "supertwisted".

The integer value in parentheses (eq 7) provides a convenient label by which to name the "supertwist state" of a nanotube according to the number of helical turns offset upon closure. Using this nomenclature, tubes with an even number of duplexes can have only even supertwist states (..., ST_{-2}, ST_0, ST_{+2},...), and tubes with an odd number of duplexes can have only odd supertwist states (..., ST_{-1}, ST_{+1},...).

To determine whether *n*HT in different supertwist states were present in our samples, we developed a method to directly measure the amount of supertwist in the DNA nanotubes. One of the DNA strands common to all *n*HT was replaced with an elongated version that had eight additional adenine bases at the 3′ end (Section 8, Supporting Information). The resulting nanotubes were similar in quality to the original, as viewed by fluorescence microscopy. We used these 8A handles as docking sites for gold nanoparticles (AuNP) that were coated with DNA strands of complementary sequence (8T).

Figure 4 shows representative TEM images of AuNP-decorated *n*HT. The distribution of their spacing indicates that each AuNP typically binds two docking sites, consistent with geometrical constraints (Section 3, Supporting Information). The distribution of their position with respect to the nanotube axis can be divided into two classes: On even-*n*HT, AuNPs lie mostly to one

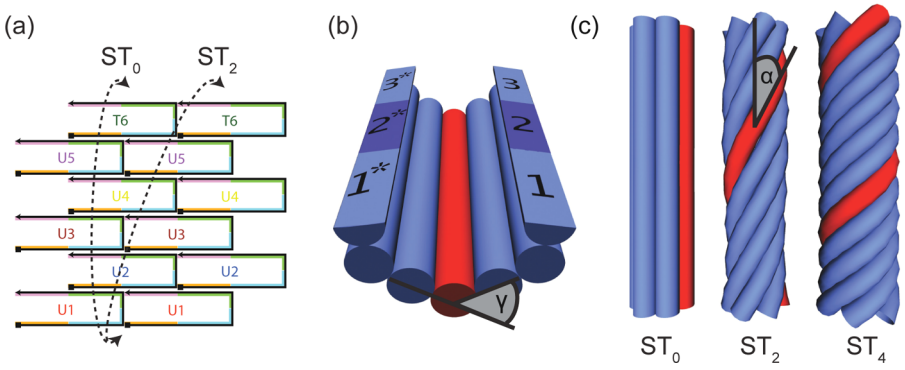

Figure 3. (a) Illustration of 6HT strand design adapted from ref 19. Each DNA strand forms a single crossover between adjacent DNA duplexes and has four binding sites, indicated by colors. (b) Cylinder model of an open DNA sheet of six double helices (cylinders) and (c) three different supertwist states of the closed DNA sheet. In (b) half-cylinders represent ssDNA, and numbers indicate domains of identical sequence (21 bases each). Hybridization of domains 1 and 1* yields ST_0, hybridization of 1 and 2* yields ST_2, and hybridization of 1 and 3* yields ST_4. The angle α, between the duplex axis and the tube axis, characterizes the supertwist. The angle γ, supplementary to the angle between successive crossovers along a given duplex, characterizes the torsional constraint imposed by the crossovers. γ takes one of the two values $\gamma = (3/8)(4\pi/21)$ and $\gamma = (11/8)(4\pi/21)$ on alternate duplexes,[19] as dictated by the number of base pairs between the crossovers, the preferred pitch of the double helix, and the angular span of the minor groove.

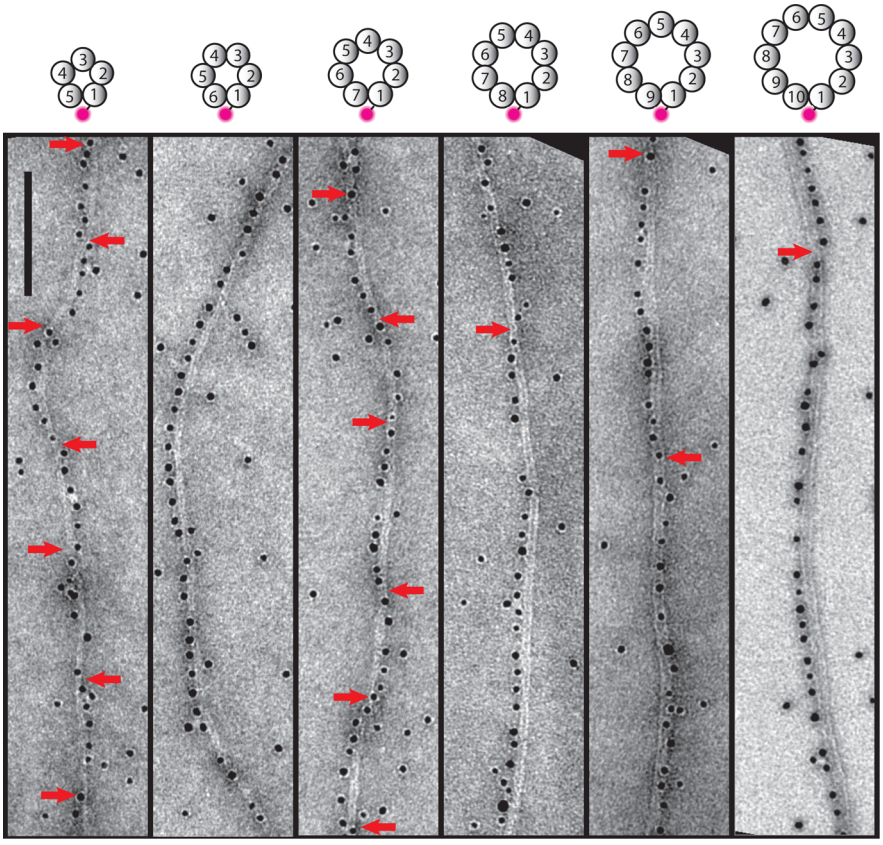

Figure 4. TEM of AuNP bound to DNA nanotubes. Red arrows indicate points where the attachment site of AuNPs crosses the tube axis. Scale bar: 100 nm.

side of the nanotube, consistent with ST_0, in which the DNA duplexes, and hence the AuNP docking sites, are parallel to the nanotube axis. Rare instances in which the line of AuNPs crosses the tube axis may be attributed to thermally excited twist of the DNA nanotube as a whole. On odd-*n*HT, by contrast, the line of AuNPs periodically crosses from one side of the tube to the other. This is consistent with finite supertwist, which appears in TEM as the 2d projection of the 3d helical path of the decorated duplex. Among the ~100 *n*HT surveyed, none had a AuNP alignment indicating supertwist higher than ST_0 for even-*n*HT and ST_1 for odd-*n*HT.

We measured the distance *d* over which AuNPs remained on one side of the *n*HT without crossing

TABLE 2. Average and Standard Deviation of the Distance *d* over Which AuNPs Remained on One Side of the *n*HT without Crossing the Tube Axis[a]

tube	$\langle d \rangle$/nm	σ_d/nm	*N*	d_{theory}/nm
5HT	81	19	23	32
6HT	246	247	17	∞
7HT	115	38	61	58
8HT	299	240	34	∞
9HT	229	94	31	94
10HT	372	173	8	∞

[a] *N* denotes the number of measurements of *d* that were taken from 2-4 different tubes per tube type. d_{theory} is the expected value of *d* based on sequence design and B-form DNA geometry.

the tube axis. For odd-*n*HT, the average $\langle d \rangle$ can be compared to a half-turn of the computed superhelical pitch for ST_1 geometry, d_{theory}. We find that on average $\langle d \rangle = 2.3 d_{theory}$ (Table 2). Hence the measured superhelical pitch is much larger than predicted by DNA sequence/geometry alone, and tubes are untwisted with respect to the geometrically predicted supertwist. For even-*n*HT we note a mismatch of more than an order of magnitude between $\langle d \rangle$ and the tube twist persistence length, P_T, expected from calculation of the polar moment of inertia (Section 6, Supporting Information, eq. S29).

To understand the observed untwisting of odd-*n*HT, the low twist persistence length of even-*n*HT, and the absence of higher supertwist states, we consider the free energy, *F*, of *n*HT relative to an open sheet of dsDNA. Again modeling the nanotube as an array of elastic cylinders, we begin by calculating the energetic costs of bending or twisting a short length, $d\ell$, of a single cylinder:[37]

$$dG_{Bend} = \frac{1}{2} B \frac{1}{r_{c,ST}^2} d\ell \quad (8)$$

$$dG_{Twist} = \frac{1}{2} C \left(\frac{d\phi}{d\ell}\right)^2 d\ell \quad (9)$$

where *B* is the bending modulus (related to the bend persistence length by $p_{Bend} = B/k_BT$), $r_{c,ST}$ is the bend radius of curvature, *C* is the twisting modulus ($p_{Twist} = C/k_BT$), and ϕ is the angle through which the cylinder is twisted about its axis.

To the extent that the cylinders are torsionally constrained, the free energy calculation should also include a twist-bend energy term:[37]

$$dG_{T\text{-}B} = \frac{1}{2} D \frac{1}{r_c^2} \frac{d\phi}{dl} \quad (10)$$

This term's linear dependence on $d\phi/dl$ breaks the degeneracy between positive and negative supertwist, favoring one particular handedness of tube supertwist. However, to our knowledge, neither the magnitude nor even the sign of the twist-bend coupling constant *D* has been determined. Furthermore, the torsional constraint imposed by crossovers between adjacent cylinders is weakened by the fact that the entire tube is free to twist about its axis, making it likely that $D_{eff} \ll D$. We therefore do not include a twist-bend energy term in our calculations.

Closing a sheet into a tube costs deformation energy ΔG whether or not the tube has supertwist. This is because each cylinder must twist, first one way and then the other, to accommodate the difference between the natural curvature of the sheet (imposed by the spacing between crossovers) and the curvature required for closure into a tube. The natural curvature of the sheet is described by the angle γ, supplementary to the angle between successive crossovers along a given duplex (Figure 3b). The sequence design is such that γ is either $(11/8)(4\pi/21)$ or $(3/8)(4\pi/21)$, depending on the duplex.[19] Assuming the closed sheet is circular

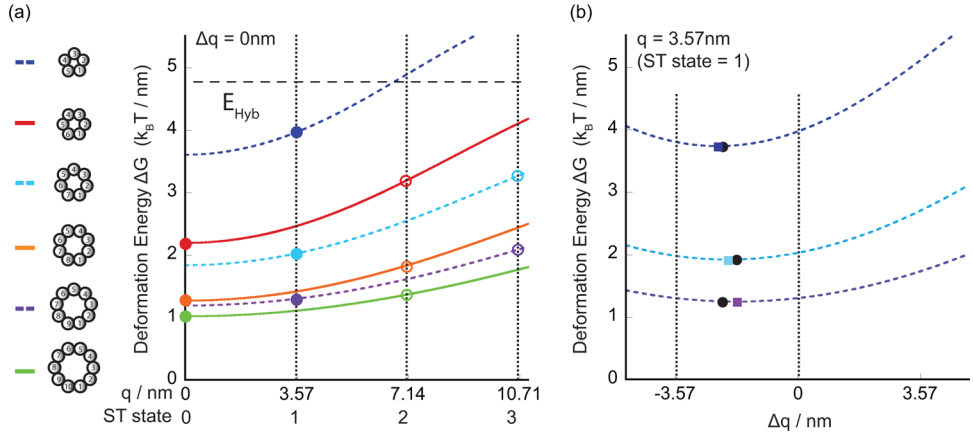

Figure 5. Plots of eq 16 using $s = 2.8$ nm, $B = 156$ pN·nm^2 (corresponding to $p_{eff} = 38$ nm), and $C = 107$ pN·nm^2. (a) Comparison of the hybridization energy gain, E_{hyb}, (horizontal dashed line) to the deformation energy cost of tube closure ΔG for *n*HT with $\Delta q = 0$ nm as a function of *q*, the edge offset, or, equivalently, the supertwist state. Geometrically calculated ST states are indicated with circles; filled circles mark the lowest energy supertwist state. (b) Deformation energy of odd-*n*HT with $q = 3.57$ nm (ST state = 1) as function of Δq with $k = 0.56 k_BT$/nm^2. Minima are highlighted with colored squares; black circles show measured untwisting. Dashed lines at $\Delta q = -3.57$ nm and $\Delta q = 0$ nm indicate full untwisting and no untwisting, respectively.

in cross-section, each duplex must twist an amount $d\phi/d\ell$, which is the difference $(2\pi/n)\cos(\alpha) - \gamma$ divided by the distance between crossovers, $\ell_0/2$ (Section 5, Supporting Information). Here, α is the angle, illustrated in Figure 3c, between cylinder axis and the tube axis:

$$\tan\alpha = \frac{q}{\pi s}\sin\left(\frac{\pi}{n}\right) \quad (11)$$

In a supertwisted tube the cylinders are bent and further twisted. Their bend is characterized by a radius of curvature $r_{c,ST} = R_{ST}/\sin^2\alpha$, making the bend energy associated with a supertwisted tube

$$dG_{Bend} = n\left[\frac{1}{2}B\left(\frac{\sin\left(\frac{\pi}{n}\right)\sin(2\alpha)\sin\alpha}{s}\right)^2\right]d\ell \quad (12)$$

The cylinders' twist is also increased by an amount $2\pi/L_{ST}$, where L_{ST} is the arc length of one helical turn of supertwist, such that the net twist of a cylinder becomes

$$\frac{d\phi}{d\ell} = \left(\frac{2\pi}{L_{ST}}\right) \pm \frac{\left(\frac{2\pi}{n}\cos\alpha - \gamma\right)}{\ell_0/2} \quad (13)$$

Here the sign of the second term alternates between successive crossovers along the cylinder. In even-*n*HT, half of the cylinders have one value of γ and half have the other. In odd-*n*HT there is one extra cylinder for which $\gamma = (3/8)(4\pi/21)$ (Section 5, Supporting Information). Therefore, the mean twist energy associated with closing a sheet into a supertwisted tube is

$$dG_{Twist} = \frac{1}{2}C\left[n\left(\frac{\sin\left(\frac{\pi}{n}\right)\sin(2\alpha)}{s}\right)^2 + \frac{n-\delta}{2}\left(\frac{\frac{2\pi}{n}\cos\alpha - \frac{4\pi}{21}\left(\frac{11}{8}\right)}{\ell_0/2}\right)^2 + \frac{n+\delta}{2}\left(\frac{\frac{2\pi}{n}\cos\alpha - \frac{4\pi}{21}\left(\frac{3}{8}\right)}{\ell_0/2}\right)^2\right]d\ell \quad (14)$$

where $\delta = 0$ for even-*n* and $\delta = 1$ for odd-*n*.

The deformation energy cost ΔG of closing a sheet of $5 \le n \le 10$ duplexes into a tube (*i.e.*, the sum of eq 12 and eq 14) is plotted in Figure 5a as a function of edge offset *q*, using values of *B* and *C* corresponding to bend and twist persistence lengths (at room temperature) of 38 and 26 nm, respectively.[38] The cost decreases with increasing *n*, as expected, because the intrinsic curvature of the duplex sheet is closest to that of a 10HT. All curves have a minimum at $q = 0$ nm, predicting that the lowest accessible supertwist state is always the most favorable to form.

We propose that the observed untwisting of odd-*n*HT is due to shearing of adjacent cylinders with respect to each other. Structurally, shearing may occur by (1) rearrangement of the phosphate backbones in the crossovers and (2) melting of base pairs flanking crossovers. Thus the energetic cost of cylinder shearing, dG_{Shear}, may have a complicated and sequence-specific dependence on the amount of shearing, Δq. For simplicity we assume a harmonic potential for dG_{Shear} with spring constant *k*:

$$dG_{Shear} = n\frac{k}{\ell_0}\left(\frac{\Delta q}{n}\right)^2 d\ell \quad (15)$$

The deformation energy is thus generalized to

$$dG(n, s, q, \Delta q) = dG_{Bend}(n, s, (q + \Delta q)) + dG_{Twist}(n, s, (q + \Delta q)) + dG_{Shear}(n, \Delta q) \quad (16)$$

Setting $2\langle d\rangle$, obtained from our TEM data, equal to the supertwist pitch (eq S21), we find that the amount of shear, Δq, necessary to yield the observed supertwist is −2.2, −1.8, and −2.2 nm for 5HT, 7HT, and 9HT, respectively. If distributed evenly across all pairs of adjacent cylinders, the required shift ($\Delta q/n = -0.44$, −0.26, −0.23 nm) is comparable to the full extent of the crossover backbone between neighboring bases. By requiring eq 16 be minimized for odd-*n*HT with $q = 3.57$ nm at the measured values of Δq we obtained the crossover spring constant $k = 0.6$, 0.7, and 0.3 k_BT/nm^2 for 5HT, 7HT, and 9HT, respectively. Using $k = 0.56\ k_BT/nm^2$ for all *n*HT yields the best fit of the minimum position of eq 16 to the measured Δq in a least-squares sense and captures all measurements to within 0.5 nm (Figure 5b).

The observation that $\langle d\rangle \ll P$ suggests that tube twist persistence length of even-*n*HT is much smaller than bend persistence length, in agreement with recent magnetic tweezers experiments on DNA origami tubes, which reported comparably low twisting rigidities.[29] This result is not consistent with a naïve twist persistence length, P_T, calculated using the polar moment of inertia of an HX-tube cross-section, which yields $P_T = 2P$ (Section S6, Supporting Information). To resolve this discrepancy, we propose that the crossovers between helices are compliant, and thus individual cylinders are able to slide relative to one another to accommodate twist. The energetic cost of this twist mode is given by eq 16, and we can approximate an associated twist persistence length P_{TS} (Supporting Information Section S6):

$$P_{TS} \lesssim \frac{1}{k_BT}\left(nC + \frac{k}{\ell_0}\frac{\pi^2 s^4}{2n\sin^4(\pi/n)}\right) \quad (17)$$

The value of $k = 0.56 k_BT/nm^2$ derived from odd-*n*HT data yields upper bounds for P_{TS} of 220, 347, and

521 nm for 6HT, 8HT, and 10HT, respectively, which easily allow for the observed tube twist.

Given k, eq 16 can be used to predict the relative abundance of supertwist states. However, a quantitative prediction depends on the shape and size of the duplex sheet that closes into a tube, which to our knowledge has not been studied for HX-tiles. We therefore limit our discussion to two cases: symmetric sheets of $n \times n$ tiles and minimal sheets ($2 \times n$ tiles). To obtain the deformation energy of a sheet, eq 16 must be multiplied by the sheet length T/ℓ_0, where T is the number of tiles. For even-nHT, neglecting supertwist states above ST_2, the probability of $ST_{\pm 2}$ is given by

$$Q_2 = \frac{2e^{(-T/\ell_0 \cdot dG_{ST2})}}{e^{(-T/\ell_0 \cdot dG_{ST0})} + 2e^{(-T/\ell_0 \cdot dG_{ST2})}} \quad (18)$$

where dG_{ST2} and dG_{ST0} are the deformation energies of ST_2 and ST_0 segments, respectively, obtained by minimizing eq 16 with respect to Δq. For $n \times n$ sheets, Q_2 is negligibly small for all nHT. For $2 \times n$ sheets, $Q_2 \leq 12\%$.

Given this probability and the finite size of our TEM data set, we considered if outliers in the persistence length measurements of individual tubes (Tables S1, S2, Supporting Information) may be due to a small fraction of tubes forming with higher supertwist states. We calculated the persistence length of a supertwisted tube by approximating the cross-section of each component cylinder in the plane perpendicular to the tube axis as an ellipse with its long axis tangential to the tube (Figure 2b). The angle α determines the length of that long axis, $r/\cos\alpha$, and the consequent increase in nanotube radius, $R_{ST} = R/\cos\alpha$, both of which factor into the area moment of inertia J (Section 4, Supporting Information) and increase the expected persistence length to

$$P(\alpha) = \frac{np_{eff}}{2}\left[\frac{1}{\cos(\alpha)^3} + \frac{1}{\cos(\alpha)} + \frac{(s/r)^2}{\sin^2(\pi/n)\cos(\alpha)^3}\right] \quad (19)$$

which simplifies to eq 5 when $\alpha = 0$. Black bars in Figure 2a mark persistence lengths calculated using eq 19 for the two lowest supertwist states for each tube type (with $s = 2.8$ nm and $p_{eff} = 38$ nm). Equation 19 predicts a persistence length increase of $\leq 25\%$ for ST_2 with respect to ST_0 tubes, too small to capture the range of observed outliers, one of which (10HT) is significantly more stiff and several of which are significantly less stiff than predicted by the fit.

We also considered whether the outliers might be a consequence of cylinder shearing, which, as in the case of twist, may enable an alternate tube bending mode. Specifically, the path length difference of the outer and inner cylinders in a bent tube may be compensated by cylinder shearing rather than stretching and compression (Section 7, Supporting Information). If cylinders must shear for a tube to bend, lowering the connection strength between cylinders should decrease tube stiffness. We experimentally tested this hypothesis by designing a modified version of 6HT, "$6HT_2$", with double strand length and thus double spacing between strand crossovers, ℓ_0. $6HT_2$ had a persistence length of only 2.1 μm (as compared to 3.3 μm of 6HT, Table 1). Thus, even though our model (eq 5), based on compression/stretching of elastic cylinders, fits the measured persistence length well (Figure 2), we cannot rule out that DNA nanotube bending also involves shearing of adjacent DNA duplexes.

Because a variety of interactions between dye molecules and DNA have been reported, we considered whether the number and relative position of the Cy3 dye we used to visualize the nanotubes were affecting our measurements. In the measurements discussed above nanotubes were labeled on only one of the n strands. This strand, called "U1", was the same in every nHT. It had a Cy3 molecule attached to one of two unpaired T-bases at its 5′ end (see Figure 3a). The remaining 42 bases of its sequence were fully embedded in the tube. A Cy3 molecule thus attached is geometrically constrained to interact within a spherical volume of radius <1 nm that intersects two DNA duplexes and a single stranded crossover between them.

To test the effect of different numbers and positions of Cy3 molecules, we prepared 6HT with Cy3 dyes on all possible subsets of U1, U4 and U5. We denote strands with Cy3 attached in subscript. Tubes with four of the seven labeling schemes ($6HT_{\{4\}}$, $6HT_{\{1,4\}}$, $6HT_{\{1,5\}}$, and $6HT_{\{4,5\}}$) had a permanent writhe shape, when imaged using time-resolved fluorescence microscopy. An example image is shown in Figure 6a. The pitch of the writhe was the same for all tubes with a specific set of labels but ranged from $\lambda = 0.7$ μm to $\lambda = 2.0$ μm for different labeling positions. Although no writhe was evident in $6HT_{\{1\}}$, $6HT_{\{5\}}$, or $6HT_{\{1,4,5\}}$, the persistence length of $6HT_{\{1,4,5\}}$, 2.7 μm, was significantly less than that of $6HT_{\{1\}}$ (3.3 μm). It is possible that this reduction in apparent stiffness is an artifact of a permanent writhe with a pitch several times the typical length of the nanotubes surveyed.

In order to understand the origin of the writhe shape, we consider that the interaction of Cy3 with the complex architecture of the DNA nanotube can result in a combination of stretch and twist deformation of the DNA within the volume accessible to the Cy3 molecule. DNA stretch and twist deformations are common for other fluorophores[41] and can be expected for Cy3 based on the finding that it can stack like an additional base pair when attached near the blunt end of a DNA duplex.[42,43] If Cy3 interacts with proximal DNA duplexes so as to stretch them, the entire tube will bend to accommodate the deformation. Similarly, if

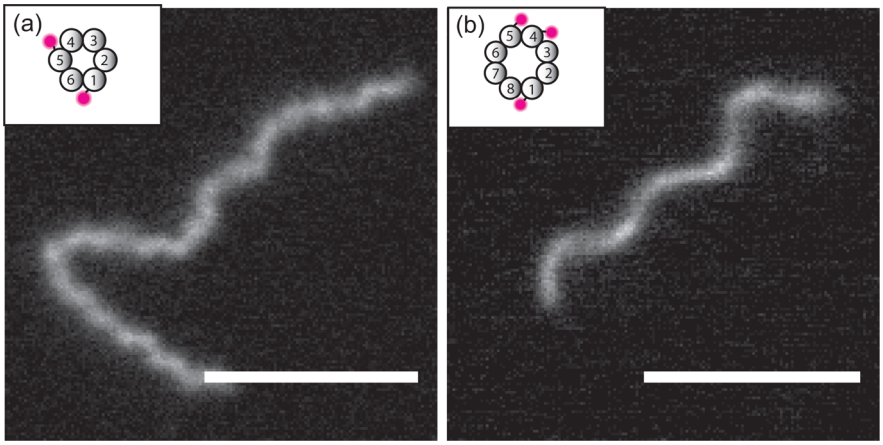

Figure 6. (a) Snapshot of a 6HT$_{\{1,5\}}$ diffusing in a PVP channel with 12 mM Mg^{2+}. The tube contour is writhed with a mean pitch of $\lambda = 0.8 \pm 0.1$ μm. (b) 8HT$_{\{1,4,5\}}$ in 39.5 mM NH_4^+ and 150 μM Mg^{2+} diffusing in a glass channel with mean pitch $\lambda = 3.5 \pm 0.6$ μm. Scale bars: 5 μm.

Cy3-exposed DNA duplexes are twisted, the entire tube will twist to accommodate. The consequence is a helical tube axis. A conceptually similar mechanism, in which excess base pairs cause bend and twist deformations, has been revealed in DNA origami and is now used in the design of intentionally curved and twisted DNA nanostructures.[26]

Since 6HT$_{\{4\}}$ is writhed but 6HT$_{\{1\}}$ and 6HT$_{\{5\}}$ are not, the magnitude of Cy3-induced deformation must depend on the local Cy3 environment (*i.e.*, base pair sequence or crossover-induced twist (γ)). Consistent with this, the strong dependence of Cy3 on its microenvironment has been observed in fluorescence lifetime, anisotropy, and quantum yield studies.[44] Interestingly, these studies found that the Cy3−DNA interaction was independent of salt concentrations over a broad range. Hence any change in nanotube structure due to salt concentration can be attributed to conformational changes of the DNA itself.

To look for such an effect, we prepared (unwrithed) *n*HT$_{\{1,4,5\}}$ in 1× TAE buffer with 12 mM $MgCl_2$ as previously described and subsequently diluted 1:80 into 40 mM NH_4OAc, resulting in final ion concentrations of 150 μM Mg^{2+} and 39.5 mM NH_4^+. In this predominantly monovalent ion solution, tubes were stable over several days and did not adhere to the glass surface of the coverslip, enabling time-resolved fluorescence microscopy without the use of polymer coating. Odd-*n*HT preserved their smooth contour, while even-*n*HT (except 6HT$_{\{1,4,5\}}$) were writhed (Figure 6b). We propose the observed writhe was induced by a change in the equilibrium helical repeat length of DNA upon ion exchange. The tube lattice may release this twist by adopting a writhe shape. Since odd-*n*HT did not display writhe, it is possible that the handedness of the twist induced by ion exchange is opposite of the existing supertwist and the two thus counteract.

CONCLUSIONS

We studied the interplay between mechanical and structural properties of DNA nanotubes. Taking advantage of the modular design afforded by HX-tiles, we systematically varied the number of DNA duplexes in a tube and used fluorescence microscopy to visualize their free-floating contours and electron microscopy to reveal supertwist of their duplex lattice.

Our measurements provide a direct reference point for the properties of more complex DNA structures. They also show that not only the shape but also the mechanical properties of DNA nanostructures can be rationally designed: the persistence length of a DNA nanotube scales accurately with its second moment of inertia when nanoscale features of the tube architecture, such as the effective stiffness of a duplex and the size of the gaps between duplexes, are considered.

Direct visualization revealed that out of the multitude of possible structures (*i.e.*, supertwist states) allowed by the tiled nature of HX-tubes, the lowest supertwist state is strongly favored. Supertwist in odd-*n*HT, forced by sequence design, is relaxed by rearrangement of the underlying DNA lattice. Twist in even-*n*HT, excited by thermal energy, appears on length scales much shorter than the bend persistence length would suggest.

We derived expressions for the elastic potential energy associated with bending and twisting cross-linked duplexes into a circular array and deformation of this array. In accordance with our data, this model predicts high twist flexibility, supertwist relaxation, and a low abundance of higher supertwist states.

For completeness, we tested mechanostructural effects of changing the density and placement of the fluorescent dye molecules we used to visualize the nanotubes and of changing the ionic conditions. We found that, under certain conditions, the nanotube axis adopts a permanent and optically resolvable writhe. This ability of extrinsic perturbations of the

DNA geometry to cause micrometer-sized deformations of the DNA nanotube, as we demonstrated by ion exchange, could be the basis for a new method for characterizing the structural consequences of a variety of biologically and medically relevant DNA-binding events.

EXPERIMENTAL METHODS

Nanotube Preparation. Samples of nanotubes ranging from five (5HT) through 10 (10HT) helices in circumference were prepared by annealing the requisite strands at 1 μM concentration (per strand) in TAE buffer with 12 mM $MgCl_2$. The anneal was performed by submerging a 200 μL PCR tube, containing between 20 and 200 μL of strand solution, in 2 L of water at 90 °C. The beaker of water was placed in a covered styrofoam box and left to cool gradually to room temperature over 48 h. A hundred times dilution (10 nM concentration per oligo) was imaged using a fluorescence microscope (Olympus IX70) equipped with a CCD camera (Hamamatsu ORCA II) and a 100×, 1.4NA oil immersion objective (Olympus PlanApo).

Two-Dimensional Sample Preparation. To avoid any flow-alignment effects (Section 1, Supporting Information) and obtain truly equilibrated conformations of DNA nanotubes in 2D, we coated the glass slide and coverslip with poly-(vinylpyrrolidone) (PVP).[45] PVP-coated slides and coverslips were gently pressed together in a home-built press and sealed with epoxy. This confined the DNA nanotubes to diffusion in a channel of less than 2 μm in height and thus kept them in the focal plane (Figure S1c). Using this method we were able to capture multiple conformations of individual tubes (typically 20−300) using a shutter with a delay time of 2−30 s to ensure that consecutive conformations are substantially different and independent of each other. A complete data set consisted of 4−13 such movies for any given tube type.

In rare instances we observed tubes that were trapped in regions where the PVP coatings of coverslip and slide contact each other. Such tubes do not display free 2D diffusion. Instead they reptate through the polymer network. This behavior is easily spotted by looking at the sum of all images in a movie. Reptating tubes appear as scraggy lines, whereas freely diffusing tubes display round and smooth intensity profiles in the image sum. Only freely diffusing tubes were chosen for analysis.

The speed of tube contour deformation depended on the height of the PVP channel and could vary from tube to tube within one channel. Analysis of correlated contours can lead to wrong persistence length estimates: a time series with finite frame number of an initially straight tube most likely yields a greater apparent persistence length than a time series of the same tube starting with a curved contour if the tube does not deform sufficiently over the duration of the time series. To avoid this effect, we obtained a separate tangent correlation function TCF(Δx,t) of every contour in a time series and computed the autocorrelation function with respect to t for $\Delta x_{min} < \Delta x < \Delta x_{max}$ in intervals of 1 μm. If the autocorrelation function exceeded the confidence bounds, a fraction of frames was removed and the process repeated until TCF(Δx,t) was uncorrelated.

AuNP Preparation. AuNP with 5 nm diameter, OD1, stabilized in citrate buffer were ordered from Sigma-Aldrich (741949). A 5.16 mL sample of 5 M NaCl was added to 10 mL of AuNP. The solution was centrifuged for 30 min at 2200 rcf. The clear supernatant was removed, and 1 mL of 1.5 mM BSPP (Aldrich 479497-1G) and 2 mL of methanol were added. The solution was centrifuged again for 30 min at 1600 rcf. The supernatant was removed, and 200 μL of BSPP was added. The concentration of AuNP was measured as 7.82 μM using a Nanodrop (ND-1000 spectrophotometer).

The 8T strand was ordered with a -thiol modification at the 5′ end. It was mixed with TCEP (Sigma 75259-1G) at final concentrations of 225 μM and 10 mM, respectively, and incubated for 30 min at room temperature. Then 20 μL of this solution was mixed with 7.67 μL of AuNP solution, and 8 μL of 100 mM citrate buffer (pH 3) and 4.3 μL of H_2O were added. After 3 min 10 μL of 500 mM HEPES (pH 7.6) was added.

To remove unbound DNA oligos, 450 μL of 1× TAE buffer was added and the solution was run through a spin filter (Amicon 100 kDa MWCO) at 10 000 rcf for 10 min. Solution that passed the filter was removed, 450 μL of fresh 1× TAE was added to the filter, and the centrifugation step was repeated. In total this centrifugation step was carried out eight times with one filter replacement after the fourth step. The concentration of DNA-coated AuNP after removing the excess DNA was measured by Nanodrop to be 1.81 μM.

A 4 μL amount of DNA nanotubes at a concentration of 100 nM per oligo (in 1× TAE with 12 mM $MgCl_2$) was mixed with 1.1 μL of coated AuNP to yield a ratio of about 1:5. The samples were incubated at room temperature for 2 h. Then 2 μL was placed on a TEM grid (Plano GmbH S162-3). After 2 min the solution was removed and the sample was stained by addition and immediate removal of a drop of 7 μL of 1% uranyl formate (UF) followed by a second UF drop, incubated on the sample for 5s.

Conflict of Interest: The authors declare no competing financial interest.

Acknowledgment. We thank A. Iteen for assistance with the fluorescence microscope, E. Roller for help preparing AuNP, and C. Riedel and S. Rubenbauer from STABLAB for help with the bootstrap method. This work was supported by National Science Foundation Award Nos. CHE-0848375 and CHE-1213895, the Volkswagen Foundation, the Kuchnir Foundation, and DFG L/1743/2-1. D.S. is grateful to the Elite Network of Bavaria (IDK-NBT) for a doctoral fellowship and to BaCaTec for travel support.

Supporting Information Available: Method: 2D confinement of DNA nanotubes using bare and PVP-coated glass; tangent correlation plots; persistence length of individual DNA nanotubes; distribution of AuNP on DNA nanotubes; persistence length model; deformation energy model; twist rigidity of DNA nanotubes; persistence length of $6HT_2$; DNA sequences; diffusion movie 10HT; diffusion movie $6HT_{\{15\}}$. This material is available free of charge *via* the Internet at http://pubs.acs.org.

REFERENCES AND NOTES

1. Seeman, N. C. Nanomaterials Based on DNA. *Annu. Rev. Biochem.* **2010**, *79*, 65–87.
2. Douglas, S. M.; Chou, J. J.; Shih, W. M. DNA-Nanotube-Induced Alignment of Membrane Proteins for NMR Structure Determination. *Proc. Natl. Acad. Sci. U.S.A.* **2007**, *104*, 6644–6648.
3. Zheng, J.; Birktoft, J. J.; Chen, Y.; Wang, T.; Sha, R.; Constantinou, P. E.; Ginell, S. L.; Mao, C.; Seeman, N. C. From Molecular to Macroscopic *via* the Rational Design of a Self-Assembled 3D DNA Crystal. *Nature* **2009**, *461*, 74–77.
4. Berardi, M. J.; Shih, W. M.; Harrison, S. C.; Chou, J. J. Mitochondrial Uncoupling Protein 2 Structure Determined by NMR Molecular Fragment Searching. *Nature* **2011**, *476*, 109–113.
5. Douglas, S. M.; Bachelet, I.; Church, G. M. A Logic-Gated Nanorobot for Targeted Transport of Molecular Payloads. *Science* **2012**, *335*, 831–834.
6. Liu, X.; Xu, Y.; Yu, T.; Clifford, C.; Liu, Y.; Yan, H.; Chang, Y. A DNA Nanostructure Platform for Directed Assembly of Synthetic Vaccines. *Nano Lett.* **2012**, *12*, 4254–4259.
7. Maune, H. T.; Han, S.-P.; Barish, R. D.; Bockrath, M.; Goddard, W. A., III; Rothemund, P. W. K.; Winfree, E. Self-Assembly of Carbon Nanotubes into Two-Dimensional Geometries Using DNA Origami Templates. *Nat. Nanotechnol.* **2010**, *5*, 61–66.
8. Tan, S. J.; Campolongo, M. J.; Luo, D.; Cheng, W. Building Plasmonic Nanostructures with DNA. *Nat. Nanotechnol.* **2011**, *6*, 268–276.

9. Kuzyk, A.; Schreiber, R.; Fan, Z.; Pardatscher, G.; Roller, E.-M.; Högele, A.; Simmel, F. C.; Govorov, A. O.; Liedl, T. DNA-Based Self-Assembly of Chiral Plasmonic Nanostructures with Tailored Optical Response. *Nature* **2012**, *483*, 311–314.
10. Steinhauer, C.; Jungmann, R.; Sobey, T. L.; Simmel, F. C.; Tinnefeld, P. DNA Origami as a Nanoscopic Ruler for Super-Resolution Microscopy. *Angew. Chem.* **2009**, *48*, 8870–8873.
11. Endo, M.; Katsuda, Y.; Hidaka, K.; Sugiyama, H. Regulation of DNA Methylation Using Different Tensions of Double Strands Constructed in a Defined DNA Nanostructure. *J. Am. Chem. Soc.* **2010**, *132*, 1592–1597.
12. Stein, I. H.; Schüller, V.; Böhm, P.; Tinnefeld, P.; Liedl, T. Single-Molecule FRET Ruler Based on Rigid DNA Origami Blocks. *ChemPhysChem* **2011**, *12*, 689–695.
13. Bell, N. A.; Engst, C. R.; Ablay, M.; Divitini, G.; Ducati, C.; Liedl, T.; Keyser, U. F. DNA Origami Nanopores. *Nano Lett.* **2012**, *12*, 512–517.
14. Wei, R.; Martin, T. G.; Rant, U.; Dietz, H. DNA Origami Gatekeepers for Solid-State Nanopores. *Angew. Chem.* **2012**, *51*, 4864–4867.
15. Rothemund, P. W. K.; Ekani-Nkodo, A.; Papadakis, N.; Kumar, A.; Fygenson, D. K.; Winfree, E. Design and Characterization of Programmable DNA Nanotubes. *J. Am. Chem. Soc.* **2004**, *126*, 16344–16352.
16. Mitchell, J. C.; Harris, J. R.; Malo, J.; Bath, J.; Turberfield, A. J. Self-Assembly of Chiral DNA Nanotubes. *J. Am. Chem. Soc.* **2004**, *126*, 16342–16343.
17. Mathieu, F.; Liao, S.; Kopatsch, J.; Wang, T.; Mao, C.; Seeman, N. C. Six-Helix Bundles Designed from DNA. *Nano Lett.* **2005**, *5*, 661–665.
18. O'Neill, P.; Rothemund, P. W. K.; Kumar, A.; Fygenson, D. K. Sturdier DNA Nanotubes *via* Ligation. *Nano Lett.* **2006**, *6*, 1379–1383.
19. Yin, P.; Hariadi, R. F.; Sahu, S.; Choi, H. M. T.; Park, S. H.; Labean, T. H.; Reif, J. H. Programming DNA Tube Circumferences. *Science* **2008**, *321*, 824–826.
20. Wang, T.; Schiffels, D.; Martinez Cuesta, S.; Kuchnir Fygenson, D.; Seeman, N. C. Design and Characterization of 1D Nanotubes and 2D Periodic Arrays Self-Assembled from DNA Multi-Helix Bundles. *J. Am. Chem. Soc.* **2012**, 1606–1616.
21. Aldaye, F. A.; Lo, P. K.; Karam, P.; Mclaughlin, C. K.; Cosa, G.; Sleiman, H. F. Modular Construction of DNA Nanotubes of Tunable Geometry and Single- or Double-Stranded Character. *Nat. Nanotechnol.* **2009**, *4*, 349–352.
22. Wei, B.; Dai, M.; Yin, P. Complex Shapes Self-Assembled from Single-Stranded DNA Tiles. *Nature* **2012**, *485*, 623–626.
23. Ke, Y.; Ong, L. L.; Shih, W. M.; Yin, P. Three-Dimensional Structures Self-Assembled from DNA Bricks. *Science* **2012**, *338*, 1177–1183.
24. Rothemund, P. W. K. Folding DNA to Create Nanoscale Shapes and Patterns. *Nature* **2006**, *440*, 297–302.
25. Douglas, S. M.; Dietz, H.; Liedl, T.; Högberg, B.; Graf, F.; Shih, W. M. Self-Assembly of DNA into Nanoscale Three-Dimensional Shapes. *Nature* **2009**, *459*, 414–418.
26. Dietz, H.; Douglas, S. M.; Shih, W. M. Folding DNA into Twisted and Curved Nanoscale Shapes. *Science* **2009**, *325*, 725–730.
27. Ke, Y.; Douglas, S. M.; Liu, M.; Sharma, J.; Cheng, A.; Leung, A.; Liu, Y.; Shih, W. M.; Yan, H. Multilayer DNA Origami Packed on a Square Lattice. *J. Am. Chem. Soc.* **2009**, *131*, 15903–15908.
28. Liedl, T.; Högberg, B.; Tytell, J.; Ingber, D. E.; Shih, W. M. Self-Assembly of Three-Dimensional Prestressed Tensegrity Structures from DNA. *Nat. Nanotechnol.* **2010**, *5*, 520–524.
29. Kauert, D. J.; Kurth, T.; Liedl, T.; Seidel, R. Direct Mechanical Measurements Reveal the Material Properties of Three-Dimensional DNA Origami. *Nano Lett.* **2011**, *11*, 5558–5563.
30. Bustamante, C.; Smith, S. B.; Liphardt, J.; Smith, D. Single-Molecule Studies of DNA Mechanics. *Curr. Opin. Struct. Biol.* **2000**, *10*, 279–285.
31. Bustamante, C.; Bryant, Z.; Smith, S. B. Ten Years of Tension: Single-Molecule DNA Mechanics. *Nature* **2003**, *421*, 423–427.
32. Bai, X.-c.; Martin, T. G.; Scheres, S. H. W.; Dietz, H. Cryo-EM Structure of a 3D DNA-Origami Object. *Proc. Natl. Acad. Sci. U.S.A.* **2012**, *109*, 20012–20017.
33. Wiggins, P. A.; van der Heijden, T.; Moreno-Herrero, F.; Spakowitz, A.; Phillips, R.; Widom, J.; Dekker, C.; Nelson, P. C. High Flexibility of DNA on Short Length Scales Probed by Atomic Force Microscopy. *Nat. Nanotechnol.* **2006**, *1*, 137–141.
34. Hagerman, P. J. Flexibility of DNA. *Annu. Rev. Biophys. Biophys. Chem.* **1988**, *17*, 265–286.
35. Furrer, P.; Bednar, J.; Stasiak, A. Z.; Katritch, V.; Michoud, D.; Stasiak, A.; Dubochet, J. Opposite Effect of Counterions on the Persistence Length of Nicked and Non-Nicked DNA. *J. Mol. Biol.* **1997**, *266*, 711–721.
36. Baumann, C. G.; Smith, S. B.; Bloomfield, V. A.; Bustamante, C. Ionic Effects on the Elasticity of Single DNA Molecules. *Proc. Natl. Acad. Sci. U.S.A.* **1997**, *94*, 6185–6190.
37. Marko, J. F.; Siggia, E. D. Bending and Twisting Elasticity of DNA. *Macromolecules* **1994**, *27*, 981–988.
38. The choice of C, slightly below the range of reported values for (un-nicked) dsDNA,[39] was based on comparison of the deformation energy to the energy gained from hybridization upon tube closure, $\Delta E_{hyb} = 4.8 k_B T$/nm, as estimated using the DINAMELT webserver[40] with $T = 49$ °C (the tube folding temperature[19]). $\Delta G - \Delta E_{hyb}$ must be negative for a sheet to close into a tube. Given that 5HT are stable, and even 4HT have been reported to form,[19] we conclude that $C_{eff} \leq 107$ pN·nm^2.
39. Bryant, Z.; Stone, M. D.; Gore, J.; Smith, S. B.; Cozzarelli, N. R.; Bustamante, C. Structural Transitions and Elasticity from Torque Measurements on DNA. *Nature* **2003**, *424*, 338–341.
40. Markham, N. R.; Zuker, M. DINAMelt Web Server for Nucleic Acid Melting Prediction. *Nucleic Acids Res.* **2005**, *33*, W577–W581.
41. Günther, K.; Mertig, M.; Seidel, R. Mechanical and Structural Properties of YOYO-1 Complexed DNA. *Nucleic Acids Res.* **2010**, *38*, 6526–6532.
42. Norman, D. G.; Grainger, R. J.; Uhrn, D.; Lilley, D. M. Location of Cyanine-3 on Double-Stranded DNA: Importance for Fluorescence Resonance Energy Transfer Studies. *Biochemistry* **2000**, *39*, 6317–6324.
43. Iqbal, A.; Arslan, S.; Okumus, B.; Wilson, T. J.; Giraud, G.; Norman, D. G.; Ha, T.; Lilley, D. M. J. Orientation Dependence in Fluorescent Energy Transfer between Cy3 and Cy5 Terminally Attached to Double-Stranded Nucleic Acids. *Proc. Natl. Acad. Sci. U.S.A.* **2008**, *105*, 11176–11181.
44. Sanborn, M. E.; Connolly, B. K.; Gurunathan, K.; Levitus, M. Fluorescence Properties and Photophysics of the Sulfoindocyanine Cy3 Linked Covalently to DNA. *J. Phys. Chem. B* **2007**, *111*, 11064–11074.
45. Srinivasan, K.; Pohl, C.; Avdalovic, N. Cross-Linked Polymer Coatings for Capillary Electrophoresis and Application to Analysis of Basic Proteins, Acidic Proteins, and Inorganic Ions. *Anal. Chem.* **1997**, *69*, 2798–2805.